Giant spin-Hall and tunneling magnetoresistance effects based on a two-dimensional nonrelativistic antiferromagnetic metal

Qirui Cui,[1,2,3] Yingmei Zhu,[1] Xiong Yao,[1] Ping Cui,[1,3] and Hongxin Yang[1,2,*]

[1]*Ningbo Institute of Materials Technology and Engineering, Chinese Academy of Sciences, Ningbo 315201, China*

[2]*National Laboratory of Solid State Microstructures, School of Physics, Collaborative Innovation Center of Advanced Microstructures, Nanjing University, Nanjing 210093, China*

[3]*Yongjiang Laboratory, Ningbo 315202, China*

(Received 15 February 2023; revised 20 June 2023; accepted 21 June 2023; published 12 July 2023)

The emergence of nonrelativistic band spin splitting in fully compensated collinear antiferromagnets provides an intriguing platform for investigating nontrivial spin-dependent phenomena. Here, we explore the relationship between magnetic symmetry and electronic states of two-dimensional (2D) antiferromagnets and demonstrate that nonrelativistic and giant band spin splitting and topological electronic features emerge in room-temperature antiferromagnetic metal V_2Te_2O that is sufficiently stable to be exfoliated from the layered compound. More interestingly, the anisotropic spin-momentum coupling of monolayer V_2Te_2O gives rise to the spin-Hall effect where the spin-charge conversion ratio is expected to be over 30%, and two fully spin-polarized and separated conduction channels with opposite spin polarization make it an ideal candidate for an electrode that is applied in the antiferromagnetic tunneling junction with large magnetoresistance. Our work elucidates the unexplored potential of 2D antiferromagnetic metals with nonrelativistic band spin splitting for their practical applications in spintronics.

DOI: 10.1103/PhysRevB.108.024410

I. INTRODUCTION

Owing to the combination of robustness against external field perturbations and ultrafast spin dynamics and switching speed, the antiferromagnets exhibiting vanished net macroscopic magnetization and negligible stray field show promise for replacing ferromagnets and being fundamental materials in magnetic memory devices with high density and low power consumption [1–17]. However, the counterpart spin degeneracy in real- and reciprocal space of conventional antiferromagnets makes the magnetic order difficult to manipulate and detect by electrical/optical approaches well applied in ferromagnets. Recently, the nonrelativistic symmetry-protected spin-split electronic band structures have been demonstrated to be able to emerge in multiple collinear antiferromagnetic (AFM) crystals [18–27]. The ferromagnetic-antiferromagnetic dichotomy in these AFM crystals leads to the term "altermagnetism" [28,29]. Moreover, such spin splitting in reciprocal space can result in nontrivial transport phenomena without the assistance of spin-orbit coupling (SOC), including spin-Hall effect (SHE) and tunneling magnetoresistance effect (TMRE), which have been well studied in the three-dimensional AFM metal RuO_2 from both theoretical and experimental aspects [30–35]. Spin current generated by SHE could be applied to switch the adjacent magnetization by generating spin torque [36–38], and TMRE underpins information processing and storage based on the magnetic tunnel junction (MTJ) where conductance is determined by the relative spin orientations of two magnetic electrodes [39–43]. Notably, layered magnets, as they possess unique features including atomic thickness, high interface quality, capability of integration in heterostructure devices, etc., provide opportunities for investigating nonrelativistic band spin splitting (NBSS) and its consequent transport phenomena, and probably lead to the development of ultracompact spintronic devices [44–49]. However, it is still challenging and interesting to realize practical applications of NBSS based on the simple and qualified two-dimensional (2D) AFM system that exhibits strong spin splitting, has sufficient spin-dependent density at the Fermi level, and possesses room-temperature structural stability and magnetic order.

In this work, we elucidate the relationship between the nonrelativistic spin-split band and magnetic symmetry in the collinear AFM monolayer, and using extensive first-principles calculations, we demonstrate that vanadium oxytelluride V_2Te_2O (VTO) is an ideal 2D AFM metal for realizing practical applications of NBSS and it simultaneously shows topological electronic features. Interestingly and importantly, the anisotropic spin splitting of electronic states gives rise to giant SHE with a spin-charge conversion ratio of over 30%, and the emergence of fully spin-polarized conduction channels makes monolayer VTO-based MTJ possibly exhibit very large TMR over 500%. These results may vastly promote the development of spintronic applications based on altermagnetic or topological metals.

II. COMPUTATIONAL METHODS

The first-principles calculations are implemented in the Vienna *ab initio* simulation package (VASP) code with density functional theory (DFT) [50–52]. The projector-augmented

*hongxin.yang@nju.edu.cn

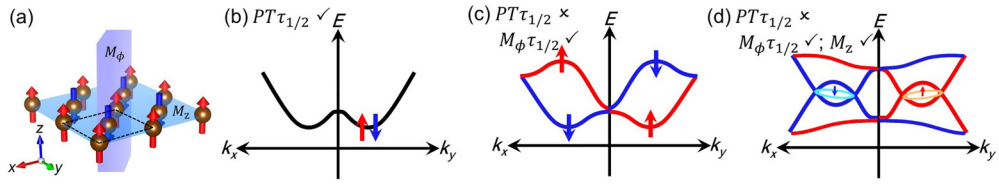

FIG. 1. (a) The schematic of a planar square lattice with *G*-type antiferromagnetism. The space group of this square lattice is *P*4/*mmm*. The Néel vector is set to be perpendicular to the material plane. Cartoons of band structure of AFM monolayer with (b) $PT\tau_{1/2}$ symmetry and (c), (d) without $PT\tau_{1/2}$ symmetry. In a 2D BZ, (c) $M_\phi\tau_{1/2}$ symmetry makes the eigenstate at $\boldsymbol{k}$ and $M_\phi\boldsymbol{k}$ exhibit the opposite spin, and (d) M_z mirror symmetry could favor M_z-protected nodal loops.

wave (PAW) method [53], and the local density approximation (LDA) are employed [54]. For describing the strongly correlated 3*d* electrons, the LDA+*U* method is applied with an effective Hubbard *U* parameter chosen to be 3 eV for transition mental elements. $U_{\text{eff}} = 2, 4$ eV are also tested, and key findings in this work are robust against U_{eff} values. Structures are fully relaxed until the force converged on each atom is less than 10^{-3} eV/Å. The plane-wave cutoff energy is set to 420 eV and Brillouin zone is sampled using Γ-centered $16 \times 16 \times 1$ and $16 \times 16 \times 5$ Monkhorst-pack *k* mesh. The optimized lattice constants of bulk VTO ($a = 3.97$ Å, $c = 12.92$ Å) are consistent with experimental results ($a_{\text{expt}} = 3.93$ Å, $c_{\text{expt}} = 13.24$ Å) [55]. To avoid interactions between adjacent layers, the vacuum space is set to be larger than 15 Å for monolayer VTO. To demonstrate the dynamic and thermodynamic stability of the monolayer VTO, we calculate the phonon band structure by using the PHONOPY code in a $4 \times 4 \times 1$ supercell [56] and perform *ab initio* molecular dynamics simulations in a canonical *NVT* ensemble for 8 ps at 500 K [57]. The detailed methods for extracting magnetic parameters are introduced in the Supplemental Material (SM) [58]. The Monte Carlo (MC) simulations with the Metropolis algorithm are applied for investigating the temperature-dependent magnetization of a $100 \times 100 \times 1$ VTO supercell, based on the explicitly resolved spin Hamiltonian. The zero-field cooling approach is adopted, and 8×10^4 time steps are employed for each temperature point in order to make the system reach thermal stability. A $260 \times 260 \times 1$ large supercell with periodic boundary is then adopted for configuring the real-space spin configurations. The spin-resolved transport properties of VTO-based MTJ are calculated using the nonequilibrium Green's function formalism (DFT+NEGF), as implemented in the ATOMISTIX TOOLKIT 2022 software package [59,60]. A 150×150 Monkhorst-Pack *k* mesh is applied in transition spectrum calculations.

III. RESULTS AND DISCUSSIONS

For understanding the nonrelativistic spin-split band in a collinear AFM monolayer, we first consider a planar square lattice with *G*-type spin configuration [Fig. 1(a)]. Space inversion symmetry *P* switches reciprocal momentum $\boldsymbol{k} \to -\boldsymbol{k}$, giving rise to $E_\uparrow(\boldsymbol{k}) = E_\uparrow(-\boldsymbol{k})$; nonsymmorphic time-reversal symmetry $T\tau_{1/2}$ switches both $\boldsymbol{k} \to -\boldsymbol{k}$ and spin state $\sigma \to -\sigma$, giving rise to $E_\uparrow(\boldsymbol{k}) = E_\downarrow(-\boldsymbol{k})$, where $\tau_{1/2}$ is the half unit cell translation along the [110] direction. Obviously, spin splitting is forbidden in the 2D Brillouin zone (BZ) [Fig. 1(b)] due to preserved $PT\tau_{1/2}$ symmetry. For achieving spin splitting, i.e., $E_\uparrow(\boldsymbol{k}) \neq E_\downarrow(\boldsymbol{k})$, nonmagnetic atoms are suggested to be inserted between magnetic atoms to break $PT\tau_{1/2}$ symmetry. Furthermore, if the modified system preserves nonsymmorphic mirror symmetry $M_\phi\tau_{1/2}$ where M_ϕ [purple plane in Fig. 1(a)] gives rise to both $\boldsymbol{k} \to M_\phi\,\boldsymbol{k}$ and $\sigma \to -\sigma$, the spin polarization of the eigenstate at $\boldsymbol{k}$ and $M_\phi\boldsymbol{k}$ should exhibit the opposite sign, i.e., $E_\uparrow(\boldsymbol{k}) = M_\phi\tau_{1/2}E_\uparrow(\boldsymbol{k}) = E_\downarrow(M_\phi\boldsymbol{k})$ [Fig. 1(c)]; if the system also preserves vertical mirror symmetry M_z [blue plane in Fig. 1(a)], the whole 2D BZ should be invariant under this mirror plane, indicating that the crossing of bands with opposite mirror eigenvalues could generate M_z-protected nodal loops [Fig. 1(d)]. The interplay between crystal symmetry and magnetic order needs to be confirmed for achieving required symmetries since spin is considered in eigenstates. For examples, the existence of $M_\phi\tau_{1/2}$ symmetry requires the Néel vector being parallel to the M_ϕ mirror plane, and the existence of M_z requires the Néel vector to be vertical to the M_z mirror plane.

Based on the above analysis, one could search or artificially design 2D AFM metals with NBSS. Considering components of the most discovered 2D van der Waals (vdW) magnets, magnetic atoms could be chosen as 3*d* transition metals whose partly occupied *d* orbitals give rise to magnetism, and bridging atoms that break $PT\tau_{1/2}$ symmetry could be chosen as VI-A and VII-A elements.

Next, we show how the spin-polarized band structure is achieved in monolayer VTO [see crystal structure in Figs. 2(a) and 2(b)] and how electronic transport behaviors are determined by unique band structure. The space group of VTO remains as *P*4/*mmm* where the magnetic V atoms are connected by nonmagnetic Te and O atoms. We adopt the spin Hamiltonian as $H = -J_1 \sum_{\langle i,j \rangle} \boldsymbol{S}_i\boldsymbol{S}_j - J_2 \sum_{\langle i',j' \rangle} \boldsymbol{S}_{i'}\boldsymbol{S}_{j'} - A\sum_i (S_i^z)^2$ for explicitly describing magnetic properties, where J_1 (J_2) is the exchange coupling between the nearest neighboring (next nearest neighboring) spin pairs, and *A* is the single-ion magnetic anisotropy. As shown in Table I, J_1 and J_2 favor AFM and FM coupling, respectively, and magnetization prefers the out of plane orientation. Based on MC simulations, we find that the Néel temperature of VTO is over 700 K (Fig. S2(a) [58]). The real-space spin configurations of VTO with a large supercell directly elucidate that the *G*-type antiferromagnetism [Fig. 1(a)] as the ground state can survive at finite temperature (Fig. S3 [58]). Importantly, $PT\tau_{1/2}$ symmetry is preserved for a pristine V lattice while it is broken for the whole system due to the existence of Te and O, which is characterized by the anisotropic magnetization density localized around V atoms [Fig. 2(b)] and largely spin-polarized band structure [Fig. 2(c)]. Electronic states exhibit totally opposite

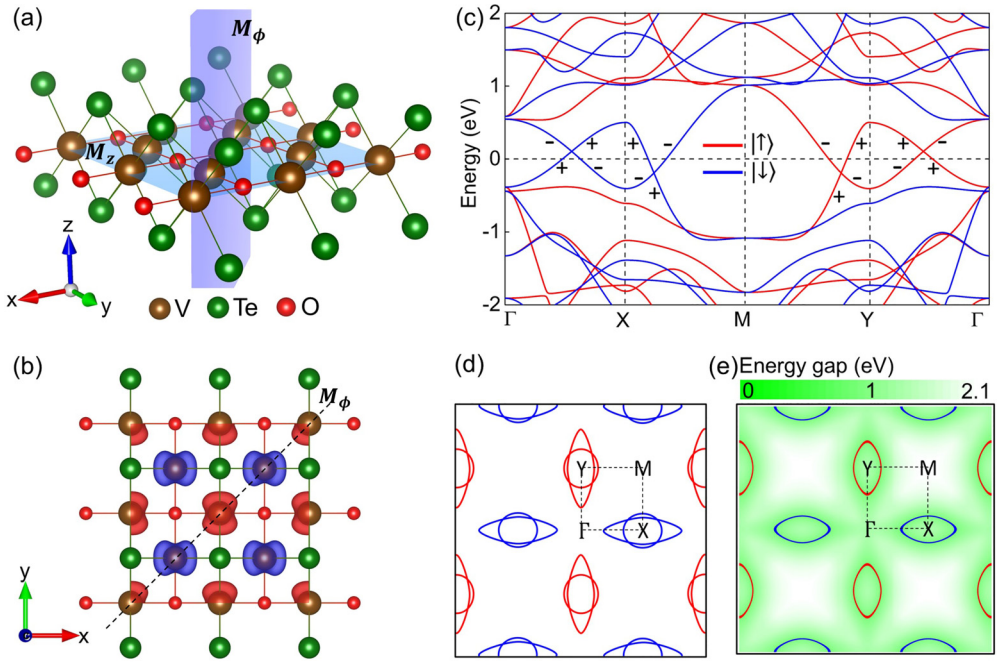

FIG. 2. The (a) side and (b) top view of crystal structure of monolayer VTO. Brown, dark green, and red balls represent V, Te, and O, respectively. Dark red and blue zones in (b) represent spin-up and spin-down magnetization densities. (c) Band structure and (d) Fermi surface. For electronic states around the X or Y point, the fully spin-polarized Fermi surface consists of two ellipses, where the flat one is dominated by the p_y or p_x orbital, and the fat one is dominated by the d_{yz} or d_{xz} orbital (Fig. S4 [58]). (e) The shape of nodal loops. The color map indicates the local gap between two crossing bands. In (c)–(e), red and blue correspond to spin-up and spin-down electronic states, respectively. DFT results elucidate that there is (b) anisotropic magnetization density in real-space and (c), (d) anisotropic spin-momentum coupling in the BZ.

spin polarization along $\Gamma \leftrightarrow X \leftrightarrow M$ and $\Gamma \leftrightarrow Y \leftrightarrow M$ due to $M_\phi \tau_{1/2}$ symmetry, and for energy level ranging from -0.38 to 0.54 eV, the spin-up and spin-down states are entirely separated in the BZ.

Figure 2(d) shows spin-polarized elliptical Fermi surfaces. The spin polarization of electronic states around the X point is perfectly compensated by that of counterpart states around the Y point. Interestingly, the crossing of p_y and d_{yz} bands, and p_x and d_{xz} bands (see orbital-resolved band structures in Fig. S4(a) [58]) generates fully spin-polarized nodal loops around the X and Y points [Fig. 2(e)]. M_z symmetry [blue plane Fig. 2(a)] is preserved since the Néel vector is perpendicular to the plane. The resulting M_z eigenvalue for holelike bands (p_y and p_x) equals $+i$, while the M_z eigenvalue for electronlike bands (d_{yz} and d_{xz}) equals $-i$ [see labels in Fig. 2(c)]. Opposite eigenvalues of crossing bands indicate that these two bands are forbidden by M_z symmetry to hybridize with each other. The p and d band crossings of VTO are thus robust against SOC effects as the Néel vector is perpendicular to the material plane (Fig. S4(b) [58]). Despite clean and fully spin-polarized nodal loops having been observed in a few FM half-metals [61–63], the coexistence of separated nodal loops with opposite spin polarization [Fig. 2(e)] in one material is reported here.

TABLE I. Structural and magnetic properties for monolayer VTO. The unit of lattice constant a is Å; the unit of magnetic moment m is μ_B; the unit of J_1, J_2 and A is meV, and the unit of Néel temperature T_N is K. The positive and negative signs of J indicate the ferromagnetic and antiferromagnetic exchange coupling, respectively, while the positive sign of A indicates the out of plane magnetization.

	a	M	J_1	J_2'	J_2''	A	T_N
V_2Te_2O	3.95	1.90	–36.79	48.15	49.24	0.36	740

The phonon band dispersion without imaginary modes (Fig. S2(b) [58]) and *ab initio* molecular dynamic simulations (Figs. S2(c) and S2(d) [58]) further demonstrate the dynamical and thermal stability of monolayer VTO, respectively. The monolayer VTO is potentially synthesized using the pulsed laser deposition. By precisely calibrating and controlling growth rate, the film thickness can be gradually reduced, thereby approaching the monolayer limit. We note that a single crystal of layered VTO (see crystal structure in Fig. S5(a) [58]) has been successfully synthesized via the topochemical deintercalation of interlayer Rb in $Rb_xV_2Te_2O$ [55]. Therefore, it is also possible to exfoliate the bulk crystal VTO down to a monolayer. Despite there being strong intralayer AFM coupling, bulk VTO exhibits paramagnetic behavior due to the very weak interlayer exchange coupling of -0.24 meV. The situation of magnetism in VTO is similar to V_2Se_2O [21,64] and VSe_2 [65], whose monolayer potentially possesses strong AFM and FM order, respectively, while the bulk is paramagnetic.

Different from reported 2D antiferromagnets with NBSS, such as semiconductor monolayer V_2Se_2O [21], semimetal monolayer CrO [26], and semiconductor bilayer CrSBr [27], robust metallic features of VTO indicate that direct electrical

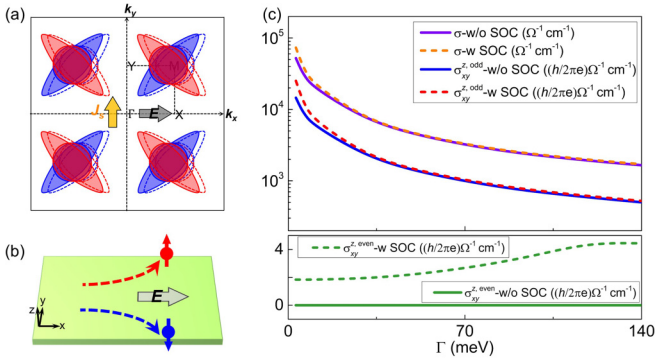

FIG. 3. (a) The electrical field $\boldsymbol{E}$ induced the Fermi surface shift for monolayer VTO with $\sqrt{2}\times\sqrt{2}\times 1$ supercell. As $\boldsymbol{E}$ is along the [100] direction, the combination of spin-up and spin-down current generates the longitudinal charge current and transverse spin current. (b) Illustration of $\boldsymbol{E}$-induced spin current in real-space. (c) Charge and spin conductivities obtained from the Kubo formula.

applications of anisotropic spin-momentum coupling can be realized since extra carrier doping is not a prerequisite for producing strong spin current. Figure 3(a) shows the spin-split Fermi surface of a $\sqrt{2}\times\sqrt{2}\times 1$ supercell of VTO. Such supercell is chosen for simplifying conductivity tensor calculations by setting the external electrical field $\boldsymbol{E}$ along the [100] direction. Due to anisotropic spin-momentum coupling, the $\boldsymbol{E}$-induced Fermi surface shift will generate (i) unpolarized longitudinal charge current and (ii) transverse pure spin current [Figs. 3(a) and 3(b)]. The response of metals to the electrical field $\boldsymbol{E}$ is well described by Kubo linear-response calculations, based on DFT electronic structures. It is approximated that the effect of disorder is a constant band broadening Γ, i.e., setting $G^R(\varepsilon)=\hbar[\varepsilon-\hat{H}+i\Gamma]^{-1}$, where G^R and $\hat{H}$ represent the retarded Green's function and Hamiltonian respectively. All linear response formulas can be spilt into two different parts which transform oppositely under the time reversal, and using constant Γ approximation, the T-odd part of Kubo formula is given by [66,67]

$$\sigma^{\text{odd}}=-\frac{e\hbar}{\pi V}\sum_{n,m,\boldsymbol{k}}\frac{\Gamma^2\text{Re}(\langle\psi_{n\boldsymbol{k}}|\hat{A}|\psi_{m\boldsymbol{k}}\rangle\langle\psi_{m\boldsymbol{k}}|\hat{v}_j|\psi_{n\boldsymbol{k}}\rangle)}{[(E_F-\varepsilon_{n\boldsymbol{k}})^2+\Gamma^2][(E_F-\varepsilon_{m\boldsymbol{k}})^2+\Gamma^2]}. \tag{1}$$

The T-even part is given by

$$\sigma^{\text{even}}=-\frac{e\hbar}{2\pi V}\sum_{n\neq m,\boldsymbol{k}}\text{Im}(\langle\psi_{n\boldsymbol{k}}|\hat{A}|\psi_{m\boldsymbol{k}}\rangle\langle\psi_{m\boldsymbol{k}}|\hat{v}_j|\psi_{n\boldsymbol{k}}\rangle)\times\left\{\frac{\Gamma(\varepsilon_{m\boldsymbol{k}}-\varepsilon_{n\boldsymbol{k}})}{[(\varepsilon_F-\varepsilon_{n\boldsymbol{k}})^2+\Gamma^2][(\varepsilon_F-\varepsilon_{m\boldsymbol{k}})^2+\Gamma^2]}\right.$$
$$\left.+\frac{2\Gamma}{[\varepsilon_{n\boldsymbol{k}}-\varepsilon_{m\boldsymbol{k}}][(\varepsilon_F-\varepsilon_{m\boldsymbol{k}})^2+\Gamma^2]}+\frac{2}{(\varepsilon_{n\boldsymbol{k}}-\varepsilon_{m\boldsymbol{k}})^2}\text{Im}\ln\frac{\varepsilon_{m\boldsymbol{k}}-\varepsilon_F-i\Gamma}{\varepsilon_{n\boldsymbol{k}}-\varepsilon_F-i\Gamma}\right\}, \tag{2}$$

where $\psi_{n\boldsymbol{k}}$ represents the Bloch function of band n, $\boldsymbol{k}$ represents the Block wave vector, e represents the elementary charge, and $\varepsilon_{n\boldsymbol{k}}$ and ε_F represent the band and Fermi energy. Under $\Gamma\to 0$ limitation, T-odd and T-even parts are further written as

$$\sigma^{\text{odd}}=-\frac{e\hbar}{2V\Gamma}\sum_{n,\boldsymbol{k}}\langle\psi_{n\boldsymbol{k}}|\hat{A}|\psi_{n\boldsymbol{k}}\rangle\langle\psi_{n\boldsymbol{k}}|\hat{v}_j|\psi_{n\boldsymbol{k}}\rangle\delta(\varepsilon_F-\varepsilon_{n\boldsymbol{k}}), \tag{3}$$

$$\sigma^{even}=-\frac{2e\hbar}{V}\sum_{n\neq m,\boldsymbol{k}}^{\substack{n\ occ\\ m\ unocc}}\frac{\text{Im}(\langle\psi_{n\boldsymbol{k}}|\hat{A}|\psi_{m\boldsymbol{k}}\rangle\langle\psi_{m\boldsymbol{k}}|\hat{v}_j|\psi_{n\boldsymbol{k}}\rangle)}{(\varepsilon_{n\boldsymbol{k}}-\varepsilon_{m\boldsymbol{k}})^2}. \tag{4}$$

The charge/spin conductivity tensor can be quantitatively estimated by setting operator $\hat{A}=\hat{v}_i/\hat{A}=\frac{1}{2}\{\hat{S},\hat{v}_i\}$. A Wannier-based tight-binding Hamiltonian is further constructed to numerically evaluate the Kubo formula, as a post-processing of DFT calculations [68]. The room-temperature (300 K) charge conductivity σ of a VTO single crystal is $6.25\times 10^3\Omega^{-1}$ cm^{-1} measured by the standard four-terminal method [55]. For broadening $\Gamma=74$ meV, σ obtained from the constant Γ approximation is very consistent with experimental results (Fig. S5(c) [58]). Since Γ of monolayer VTO still cannot be estimated quantitatively due to the lack of correlated experiments, we show conductivities as functions of Γ ranging from 0 to 140 meV [Fig. 3(c)]. Nonrelativistic T-odd spin conductivity $\sigma_{xy}^{z,\,\text{odd}}$ reaches to 9.30×10^2 $(h/2\pi e)\Omega^{-1}$ cm^{-1} for $\Gamma=74$ meV. The labels x, y, and z of $\sigma_{xy}^{z,\,\text{odd}}$ correspond to the direction of external electrical field, transverse spin current, and spin polarization of the spin current, respectively. The combination of $P4/mmm$ crystal symmetry and G-type antiferromagnetism [Fig. 1(a)] only allows $\sigma_{xy}^{z,\,\text{odd}}$ $(=\sigma_{yx}^{z,\,\text{odd}})$ as nonzero components in the spin conductivity tensor when SOC effects are not included [31]. Equation (S3) indicates that $\sigma_{xy}^{z,\,\text{odd}}$ diverges under $\Gamma\to 0$ limitation, while Eq. (S4) indicates that T-even spin conductivity $\sigma_{xy}^{z,\,\text{even}}$ converges to a finite value, which is confirmed by DFT results [Fig. 3(c)]. Notably, $\sigma_{xy}^{z,\,\text{odd}}$ is significantly enhanced to 6.01×10^3 $(h/2\pi e)\Omega^{-1}$ cm^{-1} when Γ decreases to 10 meV, and its magnitude stays much larger than $\sigma_{xy}^{z,\,\text{even}}$ by at least two orders of magnitude. The spin conductivity of widely used spin current generator Pt is around 2×10^3 $(h/2\pi e)\Omega^{-1}$ cm^{-1} [69]. Achieving strong intrinsic contribution ($\sigma_{xy}^{z,\,\text{even}}$) to SHE requires materials that possess very strong SOC, thus limiting T-even spin-charge conversion in $3d$ metals. This limitation is naturally overcome for T-odd spin-charge conversion since the SOC impact on $\sigma_{xy}^{z,\,\text{odd}}$ is very weak [see blue solid and red dashed lines in Fig. 3(c)]. Moreover, we find that T-odd spin-charge conversion ratio $\sigma_{xy}^{z,\,\text{odd}}/\sigma$ is stabilized around 31% when Γ exceeds 10 meV [Fig. 4(a)], and it could be further enhanced to be around 35% when the Fermi level is slightly shifted down [Fig. 4(b)]. Spin-charge

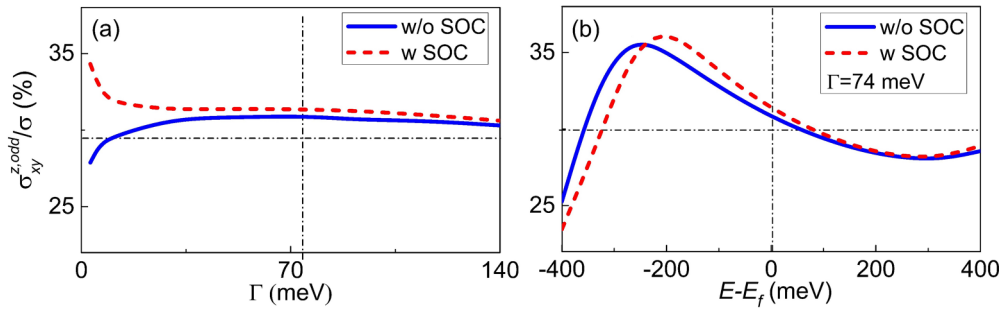

FIG. 4. The spin-charge conversion ratio $\sigma_{xy}^{z,\,\mathrm{odd}}/\sigma$ for monolayer VTO as functions of (a) Γ magnitude and (b) energy level.

conversion efficiency of monolayer VTO is even comparable with state of the art heavy metal β-W ($\sim$ 33%) [70], diluted alloy CuTb ($\sim$ 35%) [71] and larger than AFM metal RuO_2 ($\sim$ 28%) [31]. The strong spin current generated by an electrical field can be applied for magnetization switching, based on VTO/insulator/ferromagnet heterostructure where tunneling spin flow from VTO induces torque acting on the ferromagnet [72].

Figures 5(a) and 5(b) illustrate another potential application of 2D AFM metals with NBSS. The vertical heterostructure combines two VTO electrodes and the insulating barrier layer to form an antiferromagnetic tunnel junction (AFMTJ). Since layered vdW materials intrinsically exhibit weak strength of interlayer interaction and the absence of dangling bonds, the insulating barrier layer could be chosen as *h*-BN with a large band gap ($\sim$6 eV) to fabricate the vdW heterostructure with VTO [73–76]. The Fermi surface [Fig. 2(d)] elucidates that electronic states with opposite spin polarization are largely separated in BZ. For the tunneling process, the spin-down states around the *X* point and the spin-up states around the *Y* point form two 100% spin-polarized conduction channels, while there is no global spin polarization in AFMTJ. Based on the Julliere model [39], the spin of electrons is conserved in the tunneling process, and the conductance for a particular spin channel is proportional to the product of the corresponding states' density of the two electrodes. As shown in Figs. 5(c) and 5(d), in the parallel configuration [Fig. 5(a)], spin-polarized conduction channels of the electrodes perfectly match, resulting in a high conductance state, and in the antiparallel configuration [Fig. 5(b)], spin polarization of states around the *X* and *Y* points switches for top VTO layer of the MTJ, and spin-polarized conduction channels are totally mismatched, resulting in the insulating state. Therefore, AFMTJ based on VTO may theoretically show large TMR. Despite very large TMR having also been predicted in MTJ where the half-metallic Heusler alloys are chosen as the electrode, the alloy interface disorder arising from the contact with the epitaxial oxide barrier significantly reduces the spin polarization and thus makes the observed TMR much smaller than predictions [77]. This shortage is circumvented in vdW MTJs with intrinsic high interfacial quality.

In order to investigate transport behavior from first-principles calculations, we establish the AFMTJ consisting of VTO, a BiOCl barrier layer, and a Ag electrode as shown in Figs. 6(a) and 6(b). The lattice mismatch between VTO and BiOCl is 2.3%, and between VTO and Ag it is 2.7%. Notably, monolayer BiOCl could be exfoliated from its bulk phase [78,79], and its band gap could reach 2.75 eV. Transition spectra at the Fermi level are shown in Figs. 6(c) and 6(d), which are obtained for parallel and antiparallel alignments of Néel vectors of VTO. For the parallel alignment, the asymmetry between $T_p^{\uparrow}$ and $T_p^{\downarrow}$ arises from the asymmetric spin conduction channels [Fig. 2(d)]. For the antiparallel alignment, the transition obviously decays due to the blocked spin conduction channels, resulting in contributions to transition only arising from states around the spin-degenerated zone. Moreover, we obtain $G_p = 1.46 \times$

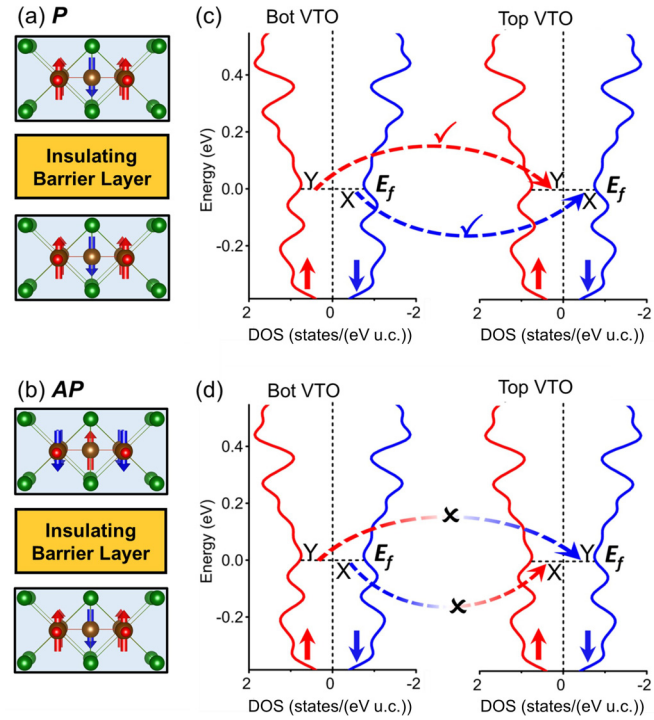

FIG. 5. The schematic of VTO/barrier/VTO AFMTJ with (a) parallel and (b) antiparallel spin configurations. Illustration of the tunneling process based on calculated density of states, for (c) parallel and (d) antiparallel states. The chosen energy level for density of states ranges from −0.38 to 0.54 eV where the spin-up and spin-down states are totally separated in the BZ. At the Fermi level, spin-down (-up) states are localized around the *X* (*Y*) point [see labels in (c)], for monolayer VTO with the spin configuration shown in (a). Once the Néel vector is reversed, the positions of spin-down and spin-up states in the Brillouin zone are consequently switched [see labels in (d)].

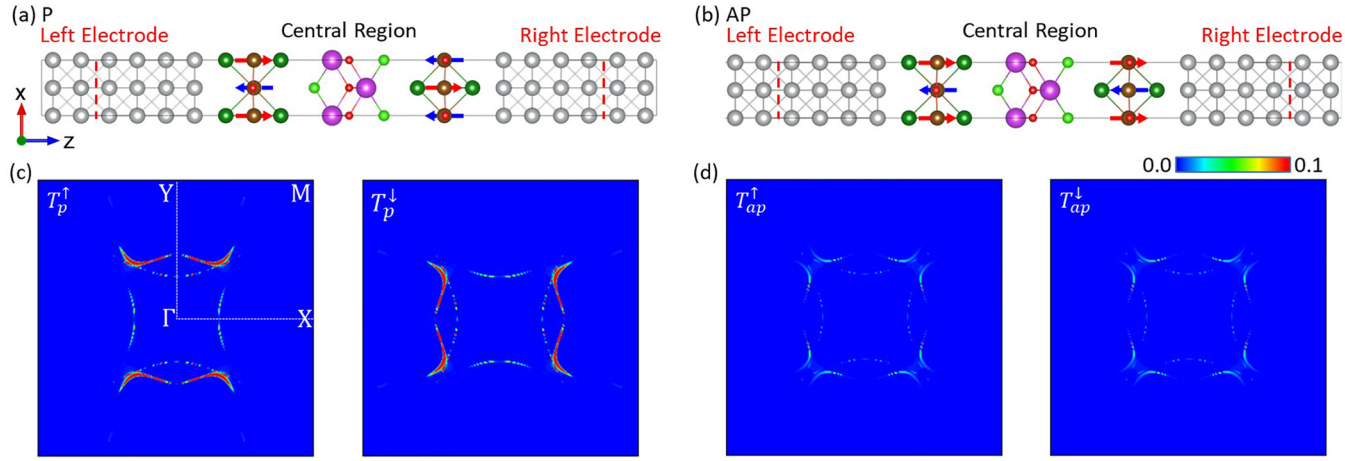

FIG. 6. The schematic structure of Ag/VTO/BiOCl/VTO/Ag AFMTJ with (a) parallel and (b) antiparallel alignment of Néel vectors of VTO. Brown, dark green, light green, red, purple, and silver balls represent V, Te, Cl, O, Bi, and Ag, respectively. The spin-resolved transition spectra in the BZ of AFMTJ with the (c) parallel and (d) antiparallel state.

10^{-7} and $G_{ap} = 2.16 \times 10^{-8}$ using the Landauer-Büttiker formula $G = (e^2/h)\sum_{\boldsymbol{k}} T(\boldsymbol{k})$ and determine that the AFMTJ possesses a large TMR ratio $(G_p–G_{ap})/G_{ap}$ reaching 574%. Further first-principles research can optimize the 2D AFMTJ design by exactly unveiling the impact of interface resistance, tunneling through the barrier evanescent state, and band structure distortion induced by the charge transfer between the electrode and barrier layer.

IV. CONCLUSIONS AND PERSPECTIVES

We highlight the impact of $PT\tau_{1/2}$, $M_\phi\tau_{1/2}$, and M_z on spin-split electronic states of the AFM monolayer and demonstrate that VTO combining the room-temperature magnetic order and structural stability meets all screening criteria for practical applications of NBSS. Nearby Fermi-level, spin-up and spin-down electronic states are totally separated in the BZ. Interestingly, the crossing of p and d bands generates two clean and fully spin-polarized nodal loops protected by M_z symmetry, and the nodal loop around the X and Y points exhibits exactly opposite spin polarization. The investigation of VTO thus expands the family of both altermagnets and topological magnetic metals. Moreover, anisotropic spin-momentum coupling gives rise to SHE dominated by T-odd spin-charge conversion, and the conversion ratio reaches over 30% which is even comparable with the record metallic systems. The emergence of fully spin-polarized conduction channels implies that monolayer VTO is an ideal electrode candidate utilized in MTJ. According to the Julliere model, it is possible to achieve a large tunnel magnetoresistance (TMR) in the VTO/barrier layer/VTO AFMTJ structure. Using the nonequilibrium Green's function formalism, we demonstrate that the TMR ratio in the Ag/VTO/BiOCl/VTO/Ag AFMTJ device reaches 574%.

Monolayer VTO preserves anisotropic band spin splitting and basically excludes spin degenerate electronic states irrelevant with spin-dependent transport [Fig. 2(c)], compared with the well-studied bulk RuO_2; unlike the AFM twisted bilayer, its structure does not need further complicated modification for generating NBSS. Since a high-quality single crystal has been synthesized, it is expected that monolayers associated with nontrivial electronic states and transport phenomena will stimulate more experimental efforts in the future. The possibility of achieving giant SHE and TMRE based on monolayer VTO means that vdW antiferromagnets show promise to be easily integrated into logic and memory technologies, and paves an avenue to design a range of competitive applications in the thickness of several atoms.

ACKNOWLEDGMENTS

This work was supported by the National Key Research and Development Program of China (MOST) (Grants No. 2022YFA405100 and No. 2022YFA1403601), the National Natural Science Foundation of China (Grant No. 12174405), Ningbo Key Scientific and Technological Project (Grant No. 2021000215), and the "Pioneer" and "Leading Goose" R&D Program of Zhejiang Province (Grant No. 2022C01053).

[1] A. H. MacDonald and M. Tsoi, Antiferromagnetic metal spintronics, Philos. Trans. R. Soc. A **369**, 3098 (2011).

[2] Y. Y. Wang, C. Song, B. Cui, G. Y. Wang, F. Zeng, and F. Pan, Room-Temperature Perpendicular Exchange Coupling and Tunneling Anisotropic Magnetoresistance in Antiferromagnet-Based Tunnel Junction, Phys. Rev. Lett. **109**, 137201 (2012).

[3] T. Jungwirth, X. Marti, P. Wadley, and J. Wunderlich, Antiferromagnetic spintronics, Nat. Nanotechnol. **11**, 231 (2016).

[4] P. Wadley, B. Howells, J. Železný, C. Andrews, V. Hills, R. P. Campion, V. Novák, K. Olejník, F. Maccherozzi, S. S. Dhesi, S. Y. Martin, T. Wagner, J. Wunderlich, F. Freimuth, Y. Mokrousov, J. Kuneš, J. S. Chauhan, M. J. Grzybowski, A. W. Rushforth, K. W. Edmonds *et al.*, Electrical switching of an antiferromagnet, Science **351**, 587 (2016).

[5] P. Tang, Q. Zhou, G. Xu, and S.-C. Zhang, Dirac fermions in an antiferromagnetic semimetal, Nat. Phys. **12**, 1100 (2016).

[6] J. Železný, P. Wadley, K. Olejník, A. Hoffmann, and H. Ohno, Spin transport and spin torque in antiferromagnetic devices, Nat. Phys. **14**, 220 (2018).

[7] R. A. Duine, K.-J. Lee, S. S. P. Parkin, and M. D. Stiles, Synthetic antiferromagnetic spintronics, Nat. Phys. **14**, 217 (2018).

[8] V. Baltz, A. Manchon, M. Tsoi, T. Moriyama, T. Ono, and Y. Tserkovnyak, Antiferromagnetic spintronics, Rev. Mod. Phys. **90**, 015005 (2018).

[9] T. Jungwirth, J. Sinova, A. Manchon, X. Marti, J. Wunderlich, and C. Felser, The multiple directions of antiferromagnetic spintronics, Nat. Phys. **14**, 200 (2018).

[10] A. Manchon, J. Železný, I. M. Miron, T. Jungwirth, J. Sinova, A. Thiaville, K. Garello, and P. Gambardella, Current-induced spin-orbit torques in ferromagnetic and antiferromagnetic systems, Rev. Mod. Phys. **91**, 035004 (2019).

[11] X. Chen, X. Zhou, R. Cheng, C. Song, J. Zhang, Y. Wu, Y. Ba, H. Li, Y. Sun, Y. You, Y. Zhao, and F. Pan, Electric field control of Néel spin–orbit torque in an antiferromagnet, Nat. Mater. **18**, 931 (2019).

[12] H. Jani, J.-C. Lin, J. Chen, J. Harrison, F. Maccherozzi, J. Schad, S. Prakash, C.-B. Eom, A. Ariando, T. Venkatesan, and G. Paolo, Radaelli antiferromagnetic half-skyrmions and bimerons at room temperature, Nature (London) **590**, 74 (2021).

[13] R. Chen, Q. Cui, L. Liao, Y. Zhu, R. Zhang, H. Bai, Y. Zhou, G. Xing, F. Pan, H. Yang, and C. Song, Reducing Dzyaloshinskii-Moriya interaction and field-free spin-orbit torque switching in synthetic antiferromagnets, Nat. Commun. **12**, 3113 (2021).

[14] L. Šmejkal, A. H. MacDonald, J. Sinova, S. Nakatsuji, and T. Jungwirth, Anomalous Hall antiferromagnets, Nat. Rev. Materials **7**, 482 (2022).

[15] H. Bai, Y. C. Zhang, L. Han, Y. J. Zhou, F. Pan, and C. Song, Antiferromagnetism: An efficient and controllable spin source, Appl. Phys. Rev. **9**, 041316 (2022).

[16] Q. Cui, Y. Zhu, Y. Ga, J. Liang, P. Li, D. Yu, P. Cui, and H. Yang, Anisotropic Dzyaloshinskii–Moriya interaction and topological magnetism in two-dimensional magnets protected by P-4m2 crystal symmetry, Nano Lett. **22**, 2334 (2022).

[17] H. Yang, J. Liang, and Q. Cui, First-principles calculations for Dzyaloshinskii–Moriya interaction, Nat. Rev. Phys. **5**, 43 (2023).

[18] L. Šmejkal, R. González-Hernández, T. Jungwirth, and J. Sinova, Crystal time-reversal symmetry breaking and spontaneous Hall effect in collinear antiferromagnets, Sci. Adv. **6**, eaaz8809 (2020).

[19] L.-D. Yuan, Z. Wang, J.-W. Luo, E. I. Rashba, and A. Zunger, Giant momentum-dependent spin splitting in centrosymmetric low-Z antiferromagnets, Phys. Rev. B **102**, 014422 (2020).

[20] I. I. Mazin, K. Koepernik, M. D. Johannes, R. González-Hernández, and L. Šmejkal, Prediction of unconventional magnetism in doped $FeSb_2$, Proc. Natl. Acad. Sci. USA. **118**, e2108924118 (2021).

[21] H.-Y. Ma, M. Hu, N. Li, J. Liu, W. Yao, J.-F. Jia, and J. Liu, Multifunctional antiferromagnetic materials with giant piezomagnetism and noncollinear spin current, Nat. Commun. **12**, 2846 (2021).

[22] M. Naka, Y. Motome, and H. Seo, Perovskite as a spin current generator, Phys. Rev. B **103**, 125114 (2021).

[23] L.-D. Yuan, Z. Wang, J.-W. Luo, and A. Zunger, Prediction of low-Z collinear and noncollinear antiferromagnetic compounds having momentum-dependent spin splitting even without spin-orbit coupling, Phys. Rev. Mater. **5**, 014409 (2021).

[24] S. A. Egorov and R. A. Evarestov, Colossal spin splitting in the monolayer of the collinear antiferromagnet MnF_2, J. Phys. Chem. Lett. **12**, 2363 (2021).

[25] Z. Feng, X. Zhou, L. Šmejkal, L. Wu, Z. Zhu, H. Guo, R. González-Hernández, X. Wang, H. Yan, P. Qin, X. Zhang, H. Wu, H. Chen, Z. Meng, L. Liu, Z. Xia, J. Sinova, T. Jungwirth, and Z. Liu, An anomalous Hall effect in altermagnetic ruthenium dioxide, Nat. Electron. **5**, 735 (2022).

[26] X. Chen, D. Wang, L. Li, and B. Sanyal, Room temperature two-dimensional antiferromagnetic Weyl semimetal CrO with giant spin-splitting and spin-momentum locked transport, arXiv:2104.07390.

[27] R. He, D. Wang, N. Luo, J. Zeng, K.-Q. Chen, and L.-M. Tang, Nonrelativistic Spin-Momentum Coupling in Antiferromagnetic Twisted Bilayers, Phys. Rev. Lett. **130**, 046401 (2023).

[28] L. Šmejkal, J. Sinova, and T. Jungwirth, Beyond Conventional Ferromagnetism and Antiferromagnetism: A Phase with Nonrelativistic Spin and Crystal Rotation Symmetry, Phys. Rev. X **12**, 031042 (2022).

[29] L. Šmejkal, J. Sinova, and T. Jungwirth, Emerging Research Landscape of Altermagnetism, Phys. Rev. X **12**, 040501 (2022).

[30] D.-F. Shao, S.-H. Zhang, M. Li, C.-B. Eom, and E. Y. Tsymbal, Spin-neutral currents for spintronics, Nat. Commun. **12**, 7061 (2021).

[31] R. González-Hernández, L. Šmejkal, K. Výborný, Y. Yahagi, J. Sinova, T. Jungwirth, and J. Železný, Efficient Electrical Spin Splitter Based on Nonrelativistic Collinear Antiferromagnetism, Phys. Rev. Lett. **126**, 127701 (2021).

[32] H. Bai, L. Han, X. Y. Feng, Y. J. Zhou, R. X. Su, Q. Wang, L. Y. Liao, W. X. Zhu, X. Z. Chen, F. Pan, X. L. Fan, and C. Song, Observation of Spin Splitting Torque in a Collinear Antiferromagnet RuO_2, Phys. Rev. Lett. **128**, 197202 (2022).

[33] S. Karube, T. Tanaka, D. Sugawara, N. Kadoguchi, M. Kohda, and J. Nitta, Observation of Spin-Splitter Torque in Collinear Antiferromagnetic RuO_2, Phys. Rev. Lett. **129**, 137201 (2022).

[34] A. Bose, N. J. Schreiber, R. Jain, D.-F. Shao, H. P. Nair, J. Sun, X. S. Zhang, D. A. Muller, E. Y. Tsymbal, D. G. Schlom, and D. C. Ralph, Tilted spin current generated by the collinear antiferromagnet ruthenium dioxide, Nat. Electron. **5**, 267 (2022).

[35] L. Šmejkal, A. B. Hellenes, R. González-Hernández, J. Sinova, and T. Jungwirth, Giant and Tunneling Magnetoresistance in Unconventional Collinear Antiferromagnets with Nonrelativistic Spin-Momentum Coupling, Phys. Rev. X **12**, 011028 (2022).

[36] J. Sinova, S. O. Valenzuela, J. Wunderlich, C. H. Back, and T. Jungwirth, Spin Hall effects, Rev. Mod. Phys. **87**, 1213 (2015).

[37] R. Ramaswamy, J. M. Lee, K. Cai, and H. Yang, Recent advances in spin-orbit torques: Moving towards device applications, Appl. Phys. Rev. **5**, 031107 (2018).

[38] C. Song, R. Zhang, L. Liao, Y. Zhou, X. Zhou, R. Chen, Y. You, X. Chen, and F. Pan, Spin-orbit torques: Materials, mechanisms, performances, and potential applications, Prog. Mater. Sci. **118**, 100761 (2021).

[39] M. Julliere, Tunneling between ferromagnetic films, Phys. Lett. A **54**, 225 (1975).

[40] J. S. Moodera, L. R. Kinder, T. M. Wong, and R. Meservey, Large Magnetoresistance at Room Temperature in Ferromagnetic Thin Film Tunnel Junctions, Phys. Rev. Lett. **74**, 3273 (1995).

[41] E. Y. Tsymbal, O. N. Mryasov, and P. R. LeClair, Spin-dependent tunnelling in magnetic tunnel junctions, J. Phys.: Condens. Matter **15**, R109 (2003).

[42] X. Chen, T. Higo, K. Tanaka, T. Nomoto, H. Tsai, H. Idzuchi, M. Shiga, S. Sakamoto, R. Ando, H. Kosaki *et al.*, Octupole-driven magnetoresistance in an antiferromagnetic tunnel junction, Nature (London) **613**, 490 (2023).

[43] P. Qin, H. Yan, X. Wang, H. Chen, Z. Meng, J. Dong, M. Zhu, J. Cai, Z. Feng, X. Zhou *et al.*, Room-temperature magnetoresistance in an all-antiferromagnetic tunnel junction, Nature (London) **613**, 485 (2023).

[44] C. Gong, L. Li, Z. Li, H. Ji, A. Stern, Y. Xia, T. Cao, W. Bao, C. Wang, Y. Wang *et al.*, Discovery of intrinsic ferromagnetism in two-dimensional van der Waals crystals, Nature (London) **546**, 265 (2017).

[45] B. Huang, G. Clark, E. Navarro-Moratalla, D. R. Klein, R. Cheng, K. L. Seyler, D. Zhong, E. Schmidgall, M. A. McGuire, D. H. Cobden *et al.*, Layer-dependent ferromagnetism in a van der Waals crystal down to the monolayer limit, Nature (London) **546**, 270 (2017).

[46] T. Song, X. Cai, M. W. Tu, X. Zhang, B. Huang, N. P. Wilson, K. L. Seyler, L. Zhu, T. Taniguchi, K. Watanabe *et al.*, Giant tunneling magnetoresistance in spin-filter van der Waals heterostructures, Science **360**, 1214 (2018).

[47] X. Wang, J. Tang, X. Xia, C. He, J. Zhang, Y. Liu, C. Wan, C. Fang, C. Guo, W. Yang *et al.*, Current-driven magnetization switching in a van der Waals ferromagnet Fe_3GeTe_2, Sci. Adv. **5**, eaaw8904 (2019).

[48] C. Gong and X. Zhang, Two-dimensional magnetic crystals and emergent heterostructure devices, Science **363**, eaav4450 (2019).

[49] Q. Cui, L. Wang, Y. Zhu, J. Liang, and H. Yang, Magnetic anisotropy, exchange coupling and Dzyaloshinskii–Moriya interaction of two-dimensional magnets, Front. Phys. **18**, 13602 (2023).

[50] G. Kresse and J. Hafner, *Ab initio* molecular-dynamics simulation of the liquid-metal–amorphous-semiconductor transition in germanium, Phys. Rev. B **49**, 14251 (1994).

[51] G. Kresse and J. Furthmüller, Efficient iterative schemes for *ab initio* total-energy calculations using a plane-wave basis set, Phys. Rev. B **54**, 11169 (1996).

[52] G. Kresse and D. Joubert, From ultrasoft pseudopotentials to the projector augmented-wave method, Phys. Rev. B **59**, 1758 (1999).

[53] P. E. Blöchl, Projector augmented-wave method, Phys. Rev. B **50**, 17953 (1994).

[54] W. Kohn and L. J. Sham, Self-consistent equations including exchange and correlation effects, Phys. Rev. **140**, A1133 (1965).

[55] A. Ablimit, Y.-L. Sun, E.-J. Cheng, Y.-B. Liu, S.-Q. Wu, H. Jiang, Z. Ren, S. Li, and G.-H. Cao, V_2Te_2O: A two-dimensional van der Waals correlated metal, Inorg. Chem. **57**, 14617 (2018).

[56] A. Togo and I. Tanaka, First principles phonon calculations in materials science, Scr. Mater. **108**, 1 (2015).

[57] S. Nosé, A unified formulation of the constant temperature molecular dynamics methods, J. Chem. Phys. **81**, 511 (1984).

[58] See Supplemental Material at http://link.aps.org/supplemental/10.1103/PhysRevB.108.024410 for (i) detailed methods for obtaining spin interaction parameters, (ii) magnetic and structural properties, (iii) supplemental band structures for monolayer VTO, and (iv) structural and electronic properties for bulk VTO.

[59] J. Taylor, H. Guo, and J. Wang, *Ab initio* modeling of quantum transport properties of molecular electronic devices, Phys. Rev. B **63**, 245407 (2001).

[60] M. Brandbyge, J. L. Mozos, P. Ordejón, J. Taylor, and K. Stokbro, Density functional method for nonequilibrium electron transport, Phys. Rev. B **65**, 165401 (2002).

[61] R.-W. Zhang, Z. Zhang, C.-C. Liu, and Y. Yao, Nodal Line Spin Gapless Semimetals and High-Quality Candidate Materials, Phys. Rev. Lett. **124**, 016402 (2020).

[62] R.-W. Zhang, X. Zhou, Z. Zhang, D.-S. Ma, Z.-M. Yu, W. Feng, and Y. Yao, Weyl monoloop semi-half-metal and tunable anomalous Hall effect, Nano. Lett. **21**, 8749 (2021).

[63] S.-S. Wang, Z.-M. Yu, Y. Liu, Y. Jiao, S. Guan, X.-L. Sheng, and S. A. Yang, Two-dimensional nodal-loop half-metal in monolayer MnN, Phys. Rev. Mater. **3**, 084201 (2019).

[64] H. Lin, J. Si, X. Zhu, K. Cai, H. Li, L. Kong, X. Yu, and H.-H. Wen, Structure and physical properties of $CsV_2Se_{2-x}O$ and V_2Se_2O, Phys. Rev. B **98**, 075132 (2018).

[65] M. Bonilla, S. Kolekar, Y. Ma, H. C. Diaz, V. Kalappattil, R. Das, T. Eggers, H. R. Gutierrez, M.-H. Phan, and M. Batzill, Strong roomerature ferromagnetism in VSe_2 monolayers on van der Waals substrates, Nat. Nanotechnol. **13**, 289 (2018).

[66] F. Freimuth, S. Blügel, and Y. Mokrousov, Spin-orbit torques in Co/Pt(111) and Mn/W(001) magnetic bilayers from first principles, Phys. Rev. B **90**, 174423 (2014).

[67] J. Železný, Y. Zhang, C. Felser, and B. Yan, Spin-Polarized Current in Noncollinear Antiferromagnets, Phys. Rev. Lett. **119**, 187204 (2017).

[68] A. A. Mostofi, J. R. Yates, G. Pizzi, Y.-S. Lee, I. Souza, D. Vanderbilt, and N. Marzari, An updated version of WANNIER90: A tool for obtaining maximally-localised Wannier functions, Comput. Phys. Commun. **185**, 2309 (2014).

[69] I. G. Y. Guo, S. Murakami, T. W. Chen, and N. Nagaosa, Intrinsic Spin Hall Effect in Platinum: First-Principles Calculations, Phys. Rev. Lett. **100**, 096401 (2008).

[70] C.-F. Pai, L. Liu, Y. Li, H. W. Tseng, D. C. Ralph, and R. A. Buhrman, Spin transfer torque devices utilizing the giant spin Hall effect of tungsten, Appl. Phys. Lett. **101**, 122404 (2012).

[71] Z. Xu, G. Dao, H. Wong, J. Tang, E. Liu, W. Gan, F. Xu, and W. S. Lew, Giant spin Hall effect in Cu–Tb alloy thin films, ACS Appl. Mater. Interfaces **12**, 32898 (2020).

[72] D. J. P. de Sousa, M. J. Sammon, R. Kim, H. Li, I. A. Young, and T. Low, Spin torque generated by valley Hall effect in WSe_2, Phys. Rev. B **106**, 184412 (2022).

[73] A. K. Geim and I. V. Grigorieva, Van der Waals heterostructures, Nature (London) **499**, 419 (2013).

[74] Y. Liu, N. O. Weiss, X. Duan, H.-C. Cheng, Y. Huang, and X. Duan, Van der Waals heterostructures and devices, Nat. Rev. Mater. **1**, 16042 (2016).

[75] J. F. Sierra, J. Fabian, R. K. Kawakami, S. Roche, and S. O. Valenzuela, Van der Waals heterostructures for spintronics and opto-spintronics, Nat. Nanotechnol. **16**, 856 (2021).

[76] T. S. Ghiasi, A. A. Kaverzin, A. H. Dismukes, D. K. de Wal, X. Roy, and B. J. van Wees, Electrical and thermal generation of spin currents by magnetic bilayer graphene, Nat. Nanotechnol. **16**, 788 (2021).

[77] K. Elphick, W. Frost, M. Samiepour, T. Kubota, K. Takanashi, H. Sukegawa, S. Mitani, and A. Hirohata, Heusler alloys for spintronic devices: Review on recent development and future perspectives, Sci. Technol. Adv. Mater. **22**, 235 (2021).

[78] J. Jiang, K. Zhao, X. Xiao, and L. Zhang, Synthesis and facet-dependent photoreactivity of BiOCl single-crystalline nanosheets, J. Am. Chem. Soc. **134**, 4473 (2012).

[79] Y. Gan, C.-W. Wu, Z.-X. Xie, Y.-X. Deng, Y. Zhang, W.-X. Zhou, and X.-K. Chen, Excellent medium-temperature thermoelectric performance of monolayer BiOCl, Langmuir **38**, 7733 (2022).